



# HRXRD and micro-CT multiscale investigation of stress and defects induced by a novel packaging design for MEMS sensors

Aurelio Borzi<sup>a,\*</sup>, Robert Zboray<sup>a</sup>, Simone Dolabella<sup>a,b</sup>, Sébastien Brun<sup>c</sup>, Florian Telmont<sup>c</sup>, Peter Kupferschmied<sup>c</sup>, Jean-François Le Néal<sup>d</sup>, Pedrag Drljaca<sup>d</sup>, Gianni Fiorucci<sup>e</sup>, Alex Dommann<sup>a</sup>, Antonia Neels<sup>a,b,\*</sup>

<sup>a</sup> Center for X-ray Analytics, Empa, Swiss Federal Laboratories for Materials Science and Technology, Überlandstrasse 129, 8600 Dübendorf, Switzerland

<sup>b</sup> Department of Chemistry, University of Fribourg, Chemin du Musée 9, 1700 Fribourg, Switzerland

<sup>c</sup> Sy&Se SA, Eplatures-Grise 17, 2300 La Chaux-de-Fonds, Switzerland

<sup>d</sup> TE Connectivity, Chapons-des-Prés 11, 2022 Bevaix, Switzerland

<sup>e</sup> Haute Ecole Arc Ingénierie/University of Applied Sciences Western Switzerland (HES-SO), Eplatures-Grise 17, 2300 La Chaux-de-Fonds, Switzerland

## ARTICLE INFO

### Keywords:

Impulse Current Bonding (ICB)

Sensors

MEMS packaging

High-resolution X-ray diffraction

Residual stress

X-ray micro-CT

## ABSTRACT

Advanced methods such as high-resolution X-ray diffraction and X-ray micro CT allow highly precise determination of materials' residual stress, volume, and lattice defects. Their conjoint exploitation offers a powering tool to facilitate the industrial implementation of novelties in microfabrication. The wafer-level packaging represents a critical step of the MEMS microfabrication resulting in a hermetic, defect- and stress-free interface. For the first time, such critical parameters are investigated related to a novel wafer-bonding process, namely Impulse Current Bonding (ICB), and compared to the standard anodic bonding technology used for MEMS production. The ICB does not induce any relevant residual stress at the interface above the limit of 1 MPa, determined by the unrivaled strain detectability of HRXRD. The bonding interface is devoid of any defects, as defined by X-ray micro-CT studies.

The ICB technology reduces the thermal budget of the packaging up to 85% compared to the anodic bonding, which outlines an outstanding step forward in reducing the energy footprint. The extension of ICB to other materials systems such as glass to ceramic or metals makes this technology a promising candidate for numerous applications, including the design of biocompatible devices for bio-implants.

## 1. Introduction

The impact of MEMS in our society can be evaluated by their presence in the ubiquitous electronic devices used every day, such as smartphones, car sensors, health care devices, and pacemakers. Sensors represent an interface between our personal life and experience and the physical world, like a smartwatch that accompanies us in every daily action offering an overview of our health state. The smart sensors market is expected to grow around 19% in 2021–2026 [1], sustained by the increase of devices' performance and efficiency. In the frame of MEMS fabrication, assembling technology plays a crucial role. The packaging has to protect the sensor against the external media all along its life and impacts critical devices' features, such as reliability, long-term stability, and total fabrication cost [2,4]. Despite this

relevance, there is only a little literature dealing with the reliability of devices' packaging since the process parameters represent sensitive information of industrial processes, remaining in general unpublished. Nevertheless, the two critical issues associated with the reliability of MEMS packaging relate to the bonding interface: it must maintain hermeticity or vacuum and not be affected by high residual stress [5,6].

First, vacuum degradation and loss of hermeticity are typically related to defects such as voids or cracks in the vicinity of the bonding interface. The vacuum's leakage might lead to severe degradation of the devices' performance, especially in the well-known MEMS application sector of gyroscopes, by lowering the quality factor (Q-factor) due to the increase of the viscous damping [7]. Also, the loss of hermeticity may result in corrosion of the active components of sensors because of the external environment. The second major issue is the residual stress

\* Corresponding authors at: Center for X-ray Analytics, Empa, Swiss Federal Laboratories for Materials Science and Technology, Überlandstrasse 129, 8600 Dübendorf, Switzerland

E-mail addresses: [aurelio.borzi@empa.ch](mailto:aurelio.borzi@empa.ch) (A. Borzi), [antonia.neels@empa.ch](mailto:antonia.neels@empa.ch) (A. Neels).

<https://doi.org/10.1016/j.apmt.2022.101555>

Received 2 February 2022; Received in revised form 26 May 2022; Accepted 9 June 2022

Available online 23 June 2022

2352-9407/© 2022 The Authors. Published by Elsevier Ltd. This is an open access article under the CC BY license (<http://creativecommons.org/licenses/by/4.0/>).

induced by the wafer bonding process due to thermal mismatch between materials and/or the generation of lattice point defects such as vacancies and interstitials [8]. Most MEMS functioning relies on delicate moving parts, which are extremely sensitive to the presence of external mechanical stress. Packaging-induced stress may translate into deleterious effects such as the resonance frequency shift or might even lead to breakage and related failure of the component itself.

In the frame of sensors fabrication, hermetic packaging can be accomplished on the wafer-level by anodic bonding (AB) of silicon and glass [9,10], a process demonstrated for the first time in the 1970ies [11]. This technology has been studied as far as some critical issues such as the bonding strength [12], interface fracture toughness [13], and induced stress [14] are concerned. According to previous studies, the packaging-induced stress is mainly due to the thermal mismatch between the bonded components [2], i.e., glass and silicon in the case of AB. Since the anodic bonding requires relatively high temperatures, typically between 300 and 400 °C, this technology forces the use of high-cost glass with a reduced coefficient of thermal expansion (CTE) being close to silicon ( $2.6 \text{ ppm.K}^{-1}$ ). Even if the utilization of expensive low-CTE glasses succeeds in reducing the packaging-induced stress, only a few studies are dealing with the reliability of the AB process in terms of degradation of the vacuum [2]. An additional limitation of the AB packaging technology is the specificity of silicon-to-glass wafers arising from the bonding mechanism.

Starting in 2015, a novel wafer bonding approach, namely the Impulse Current Bonding, has been developed. It was patented in Europe (EP3320403-B1) and the US (US 10,788,793-B2). The ICB assembling mechanism is attributed to be different from the current AB. Even if not fully understood yet, it enables remarkable advantages over the other well-established packaging design technologies. Firstly, the ICB involves a substantially lower process temperature, starting from 118 °C, compared to anodic bonding. The temperature reduction relieves the concerns related to the CTE mismatch between the bonded materials and consequently the process-induced residual stress. In addition, the duration of the bonding process is around 150 s versus 300 s typically required for AB, both translating into a reduction of the energy consumption. The resulting throughput of the ICB technology is highly appealing for industries as it will increase productivity. The electrical energy consumption is supposed to remain unchanged, even if the novel approach is based on pulsed current instead of a long-time pulse for AB known to ensure a continuous alkali-cation migration until saturation. A substantially lower process temperature and duration of the ICB microfabrication has a remarkable positive impact in limiting the overall energy consumption and, consequently, environmental footprint. When considering the maximum temperature and duration of the bonding process, the ICB reduces the thermal budget by 70–85% compared to the AB. Considering the extension and constant growth of the sensors market, the impact obtainable from this outstanding reduction of energy consumption becomes immediately apparent. Besides the primarily relevant benefit to the environment, reducing energy consumption adds to the possible use of higher-CTE and less expensive glass materials for an undoubted economic advantage. Resultantly, a substantial cost-benefit could be achieved for mass-scale production while guaranteeing the high quality and reliability of the packaging. Another advantage of this novel approach is related to the wide range of materials classes that can be bonded using the novel ICB process, such as glass-to-metal or glass-to-ceramics. All the mentioned advances position the ICB in the trend of low-temperature bonding considered to have the potential to push electronic and optoelectronic capabilities in a More-than-Moore law ability [15]. Material versatility, low-temperature processes, and moderate material roughness requirements qualify the ICB technology also promising in applications outside the semiconductor area. ICB could solve frequently occurring issues for industrial equipment, for rapid connectivity, and guaranteeing a permanent hermeticity.

Considering the novelty of this technology, evaluating the influence of the process on materials-related properties such as residual stress,

lattice defects, and volume damages at the bonding interface plays a crucial role in assessing the quality and reliability of a packaging process. In particular, while the decrease in process temperature and duration enables the reduction of the thermal budget of the ICB process, the decreased atomic diffusivity at a lower temperature [16] partially inhibits recrystallization processes and limits the related removal of defects. Consequently, a higher defect density is expected to affect materials processed by ICB compared to the AB process. In this respect, X-ray-based analytical methods constitute potential tools in the hands of researchers and process engineers. They are non-destructive and reveal materials features in a wide range of scales, from 3D-volume voids and cracks in the micrometer (or larger) scale down to lattice defects at the nanoscale. X-ray diffraction (XRD) is one of the most established methods for microstructural investigations and the study of order-disorder transitions [17], chemical composition and crystalline phases, preferred orientation and texture [18], the size of crystallites [19–21], microstrain, and defects densities and mobility [21–23]. The extensive processing and utilization of bulk single crystals and high-quality epitaxial thin films by the microelectronic industry led to the improvement of the analytical performances of XRD instruments, opening the floor to high-resolution X-ray diffraction (HRXRD) [23–29]. HRXRD is a powerful method for exploring the microstructure or highly ordered systems because of its unrivaled high lattice strain sensitivity. In our previous work, HRXRD was exploited to analyze epitaxial thin films of ceramic materials for optoelectronics to study the influence of the optimization of the deposition parameters on the materials microstructure [21]. Dolabella et al. applied HRXRD to a new type of nanowire system in order to study the influence of critical steps of the fabrication process, such as electron-beam lithography and deep reactive ion etching [30]. In Yildirim et al., the microstructural investigation of nanometer-thick Pt layer revealed fundamental for evaluating the performance of a novel deposition method [31]. Strain and stress affecting material crystal lattices and their relationship with devices reliability were evaluated in Si-based MEMS for sensing applications [32], and the correlation with the wafer bonding process was assessed [33]. The high instrumental resolution translates into the possibility to measure the residual stress in highly crystalline materials up to the MPa level. However, as the strain/stress detection threshold and resolution depend also on the physical and microstructural features of materials, such as mechanical properties and crystallinity. Poor crystallinity and high density of defects broaden the XRD peak profile, which downgrades the resolution with respect to lattice strain and residual stress determination.

X-ray micro-CT has seen a period of rapid growth over the last 20 years and is routinely applied to commonly available tools within materials science laboratories. This is due to considerable improvements achieved in spatial resolution and image reconstruction time and the increasing availability of commercial instruments. Micro-CT can deliver the 3D (volume) distributions of different material features such as inclusions and matrix morphology [34], cellular morphology, porosity, transport processes in solutions [35], defects, and fibrous structure morphology [36] at single-digit micrometer scales. For recent reviews for material science application, see e.g. [37–39]. X-ray micro-CT can also be applied to investigate the interface of bonded wafers to reveal the presence of defects or voids, which are responsible for the lack of hermeticity, one of the two above-mentioned critical issues affecting the packaging.

In our previous work, the conjoint exploitation of HRXRD and micro-CT enabled the characterization of the defective status of a silicon-to-sapphire bonded system at the micron- and nanoscale [40]. The status of materials at the bonding interface is observed by X-ray micro-CT. HRXRD enables accessing crucial information, such as the strain and stress, the presence of defects by means of evaluation of the Bragg's reflections positions and widths, and the presence of diffuse X-ray scattering (DXS). Here, we aim to evaluate the impact of the novel process on the status of the materials involved in the bonding, i.e.,

silicon and borosilicate glass, on a comparative scale with respect to the conventionally and worldwide exploited anodic bonding process.

## 2. Materials and methods

ICB processed samples consist of a CZ Silicon (100) p-type 650  $\mu\text{m}$  thick wafer bonded with a 500  $\mu\text{m}$  thick borosilicate glass at a temperature of 160  $^{\circ}\text{C}$  for a cycle duration of 150 s. The process is based on impulse current involving a high atomic flow rate at the interface during the oxidation process that limits the needed temperature. After the bonding, the wafer stack is diced mechanically with a standard resinoid saw blade for obtaining squared samples of  $2 \times 2 \text{ cm}^2$ .

Samples processed by anodic bonding consist of a CZ Silicon (100) p-type 650  $\mu\text{m}$  thick wafer bonded to a 500  $\mu\text{m}$  thick borofloat glass wafer. The bonding process is performed anodically, applying a temperature typically between 300 and 400  $^{\circ}\text{C}$ , and a high voltage between 1000 and

1500 V. The temperature will increase the ion mobility within the glass wafer. In contrast, the high voltage will force the oxygen atoms in the glass to bond with the silicon atoms of the silicon wafer. After bonding, squared samples of  $2 \times 2 \text{ cm}^2$  are obtained through the previously described procedure.

The glass thickness was reduced to a final value equal to 39  $\mu\text{m}$  by etching with HF for enabling X-ray diffraction measurements of the bonding interface. This allows releasing the stress related to the thermal mismatch, which does not represent a concern in the case of Si and high-quality, low CTE borosilicate glass, and more importantly, enables the analysis of stress due to lattice defects generation.

High-resolution X-ray diffraction (HRXRD) measurements were performed using a BRUKER D8 Discover DaVinci instrument equipped with high-resolution optics for the primary and scattered beam, as shown in Fig. 1(b). The X-ray beam is generated by a Cu-sealed source and collimated by a Göbel mirror. A Bartels four-crystal symmetrical Ge

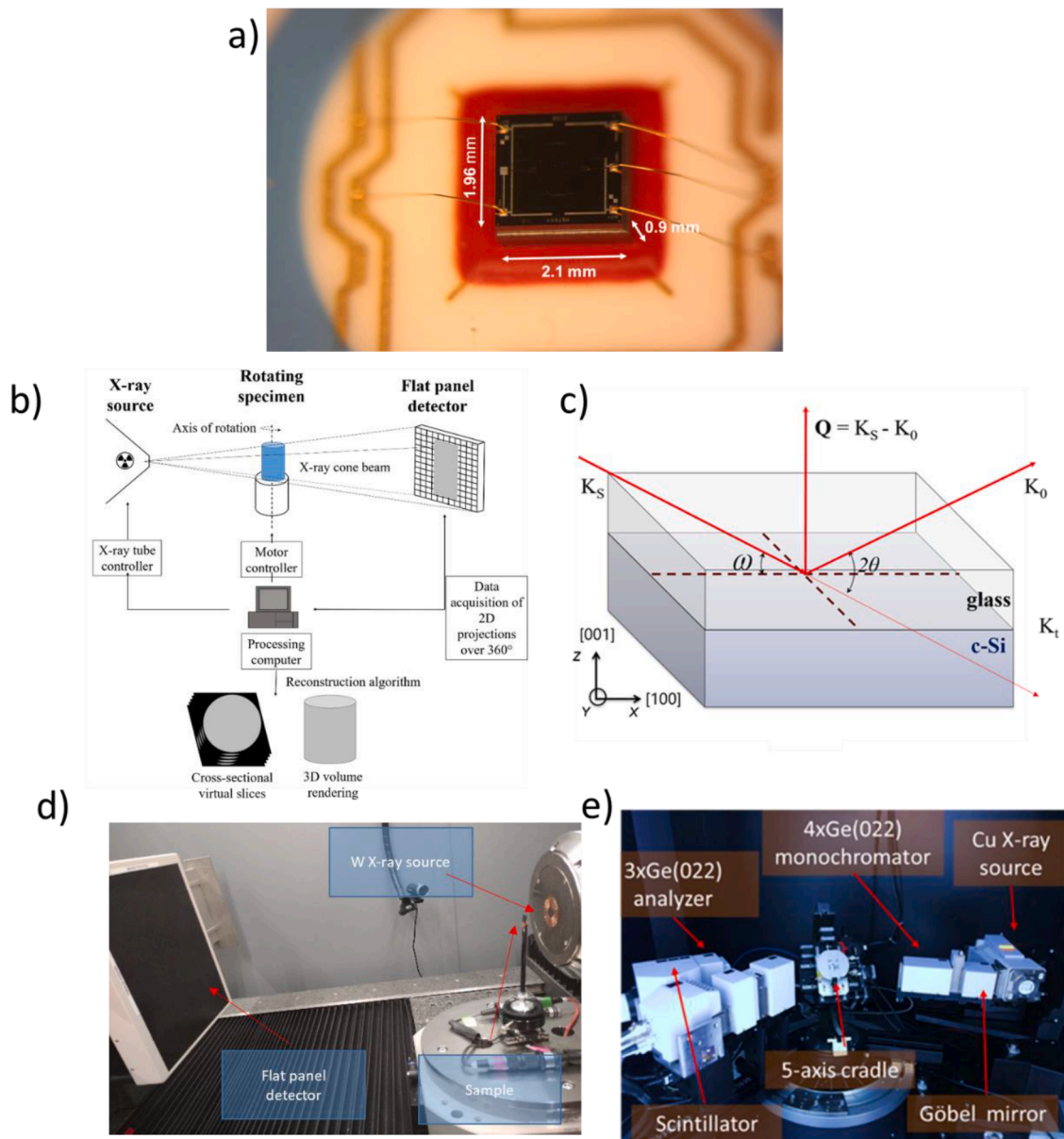


**Fig. 1.** (a) Pressure sensor prototype assembled by the ICB technology; (b) X-ray micro-CT experimental setup; (c) HRXRD experimental configuration with the most important exploited angles; (d) inside the cabinet of an RX Solution Easytom XL micro/nano CT on the left with the flat panel detector, and the nano and micro-focus X-ray tubes on the right, and in the middle below the rotating sample; (e) BRUKER D8 Discover DaVinci equipped with high-resolution optics of the primary beam (Goebel mirror and Bartels monochromator) and diffracted beam (3xGe(022) crystal analyzer)

(022) monochromator is mounted to limit the energy and angular acceptance of the primary beam. A triple-crystal symmetrical Ge(022) crystal analyzer is mounted in front of the scintillator detector to reduce the angular and energetic acceptance. The angular resolution depended on the Bragg angle and was determined before each measured reflection using the instrument manufacturer's 3 mm-thick stress-free SCSi reference sample. The instrumental resolution was determined by the measurements of the rocking curves of the Si 004 reflection in symmetric coplanar diffraction geometry, Si 113, and Si 111 in symmetric noncoplanar diffraction geometry. The same reflections are taken into account in the experimental procedure on the assembled samples. Instrumental broadenings are determined with  $2.5 \times 10^{-3}$  for the 004 reflection and  $3.0 \times 10^{-3}$  and  $3.3 \times 10^{-3}$  for the 113 and 111 reflections, respectively. The instrumental resolutions for each measured reflection are reported in Table 1, and the derived resolution is in terms of strain detection.

Materials microstructure was investigated by performing scans along the radial direction, i.e.,  $\omega$ -2 $\theta$  scan, the angular direction, i.e.,  $\omega$ -rocking curves (RCs), and Reciprocal Space Maps (RSMs), i.e. ( $\omega + \omega_0$ )-2 $\theta$  scans at different  $\omega_0$  offset. The width of the line beam in the scattering plane was selected using a 600  $\mu\text{m}$  slit and kept constant for each measurement. Considering the diffractometer's geometrical features, the beam's footprint on the sample surface was determined by the relationship  $S = \frac{w}{\sin(\alpha)}$ , related to the slit size,  $w$ , and the incidence angle  $\alpha$ .  $S$  is calculated with 1.06, 1.28, and 2.44 mm for the 004, 113, and 111 reflections, respectively. Given the slight divergence of the beam and high movement precision ( $\pm 0.0001^\circ$ ), the only source of noticeable error on these values is related to the uncertainty on the width of the slits. These high-precision optics typically have a tolerance of  $\pm 1 \mu\text{m}$  over the nominal aperture, which impacts on the final value of  $L$  for not more than  $\pm 4 \mu\text{m}$ . The length of the beam in the direction perpendicular to the scattering plane is reduced to 2 cm using vertical slits. The irradiated surface is calculated to be 21.2, 25.5, and 48.8  $\text{mm}^2$  for the 3 reflections. The calculation of the irradiated volume can only be estimated, which is related to the uncertainty over the thickness of the residual glass after etching. However, we know the X-ray penetration depth in silicon according to the mass attenuation coefficient of silicon [41]. At an energy of 8 keV, X-rays travel about 70  $\mu\text{m}$  into silicon [37,38] which corresponds to a penetration depth of only 17.2, 32.9, and 39.7  $\mu\text{m}$  when the Si 111, Si 113, and Si 004 reflections are considered. Accordingly, the irradiated volume is about 0.84  $\text{mm}^3$  for all three exploited reflections. The relationship between the measured reflections and the surface and volume of the sample probed are reported in Table 1. The HRXRD experimental configuration with respect to the investigated angles of interest is shown in Fig. 1(c).

For the ICB process, two samples coming from different parts of the bonded and diced wafer, and with different thicknesses of the residual glass (39 and 72  $\mu\text{m}$ ) have been investigated. No significant differences in terms of conservation of the microstructure have been found. The results presented in this work are related to the sample with the thinner residual glass.

**Table 1**

Primary information about the angular and strain resolutions and the surface and volume of silicon probed by X-rays. Reference values measured on a stress-free Si 111 crystal.

Reflection hkl	FWHM* of a reference Si crystal ( $^\circ$ )	Strain limit	Incidence angle to the atomic plane family <hkl> ( $^\circ$ )	Beam footprint on the sample surface ( $\text{mm}^2$ )	Penetration depth ( $\mu\text{m}$ )	Irradiated volume ( $\text{mm}^3$ )
Symmetric 004	0.0025	$\pm 6 \times 10^{-6}$ (out-of-plane)	34.565	21.2	39.7	0.84
Asymmetric 113	0.0030	$\pm 2 \times 10^{-5}$ (in-plane)	28.061	25.5	32.9	0.84
Asymmetric 111	0.0033	$\pm 8 \times 10^{-5}$ (in-plane)	14.221	48.8	17.2	0.84

\* FWHM = full width at half maximum

For the X-ray micro-CT investigations, we have been using an EasyTom XL Ultra 230-160 micro/nano-CT scanner (RX Solutions SAS, Chavanod, France). The scanner features a Hamamatsu open-type, reflection micro-focus X-ray tube, as in Fig. 1(d). The scan for the entire sample was performed using a Varian PaxScan 2520DX detector (flat panel with amorphous silicon and a CsI conversion screen;  $1920 \times 1536$  pixel matrix; pixel pitch of 127  $\mu\text{m}$ ; 16 bits of dynamic range). The tube was operated at 70 kV and a current of 200  $\mu\text{A}$ . The isotropic voxel size of the CT scan was 7.98  $\mu\text{m}$ . The actual image resolution was estimated to be 17.8  $\mu\text{m}$  by fitting a logistic function over an edge in the reconstructed grey-scale CT slice image. The images were acquired at 7.0 frames per second speed and averaging 15 frames per projection. Furthermore, a local CT has been carried out over a small region of interest (ROI) in the center of the specimen (see in red in Fig. 3(e)) to check the bonding quality and potential presence of small cracks and defects at significantly higher resolution. For this, a transmission-type Hamamatsu nano-focus tube operated with a LaB<sub>6</sub> cathode and a 1  $\mu\text{m}$ -thick tungsten target, also available in the scanner, was used. It enables a much smaller X-ray focal spot and higher resolution compared to the micro-focus tube; the tube was operated at 90kV and a target current of 50  $\mu\text{A}$ . The same detector was used at 2.0 frames per second speed averaging 8 frames per projection. The isotropic voxel size of the local CT scan was 1.55  $\mu\text{m}$ , whereas the actual image resolution was estimated to be 3.5  $\mu\text{m}$ .

Image analysis has been carried out using the commercial software package VG Studio Max 3.3 [17].

Strain ( $\epsilon$ ) is defined as a structural deformation that a material undergoes in response to an applied stress ( $\sigma$ ) [42]. This stress can be applied from external forces on the material, as well as can be due to structural lattice defects such as interstitial or vacancies [8]. Mathematically the stress is described by a second-rank tensor with elements

$$\epsilon_{kl} = \frac{1}{2}(e_{kl} + e_{lk}) \quad (1)$$

where  $e_{kl} = \frac{\partial u_k}{\partial x_l}$ , with  $\partial u_k$  being the component of the displacement vector  $u(x_1, x_2, x_3)$  along the Cartesian direction  $x_l$ ,  $l = 1, 2, 3$ . If the deformation of the material is limited to the elastic regime, the module of the strain relates to the applied stress by the Hooke's law,  $\sigma_{ij} = c_{ijkl}\epsilon_{kl}$ , where the two-rank tensors of the stress and strain are in relationships by the fourth-rank stiffness tensor,  $c_{ijkl}$ .

When analyzing the status of the stress in materials undergone the wafer bonding process, the external stress due to the mismatch between the coefficients of thermal expansion (CTE) of the participating materials has to be considered. However, in the present case, this external source of stress is negligible based on (i) the very low CTE mismatch between the high-quality glass used and silicon and (ii) the thermal stress depending on the volumes of materials. It means that the already minor thermal stress has been released during the glass etching process. This enabled the analysis of the stress due to the formation of crystalline defects at the bonding interface in relation to the bonding process.



In this work, we determined the strain along the X, Y, and Z directions of the system corresponding to the [100], [010], and [001] crystalline directions, respectively. The case of plane stress was applied to our samples. Under this assumption, the only non-zero components of the stress are in the same plane. In the case of plane stress, the relationship between strain and stress along the crystalline directions writes

$$\varepsilon_x = \frac{\sigma_x}{E_x} - \nu_{xy} \frac{\sigma_y}{E_y} \quad (2)$$

and

$$\varepsilon_y = \frac{\sigma_y}{E_y} - \nu_{yx} \frac{\sigma_x}{E_x} \quad (3)$$

In the case of silicon (Si), the Young modulus,  $E$ , and Poisson's coefficient,  $\nu$ , along the directions of interest are [43,44]  $E_x = E_y = E_z = 130 \text{ GPa}$ , and  $\nu_{xy} = \nu_{yx} = 0.28$ , respectively.

Accordingly, when the stress along the X and Y directions is equal, the strain along these directions writes as follows:

$$\varepsilon_x = \varepsilon_y = \sigma_{xy} \frac{1 - \nu_{xy}}{E} \quad (4)$$

Moreover, if the strain in-plane is experimentally determined, as in

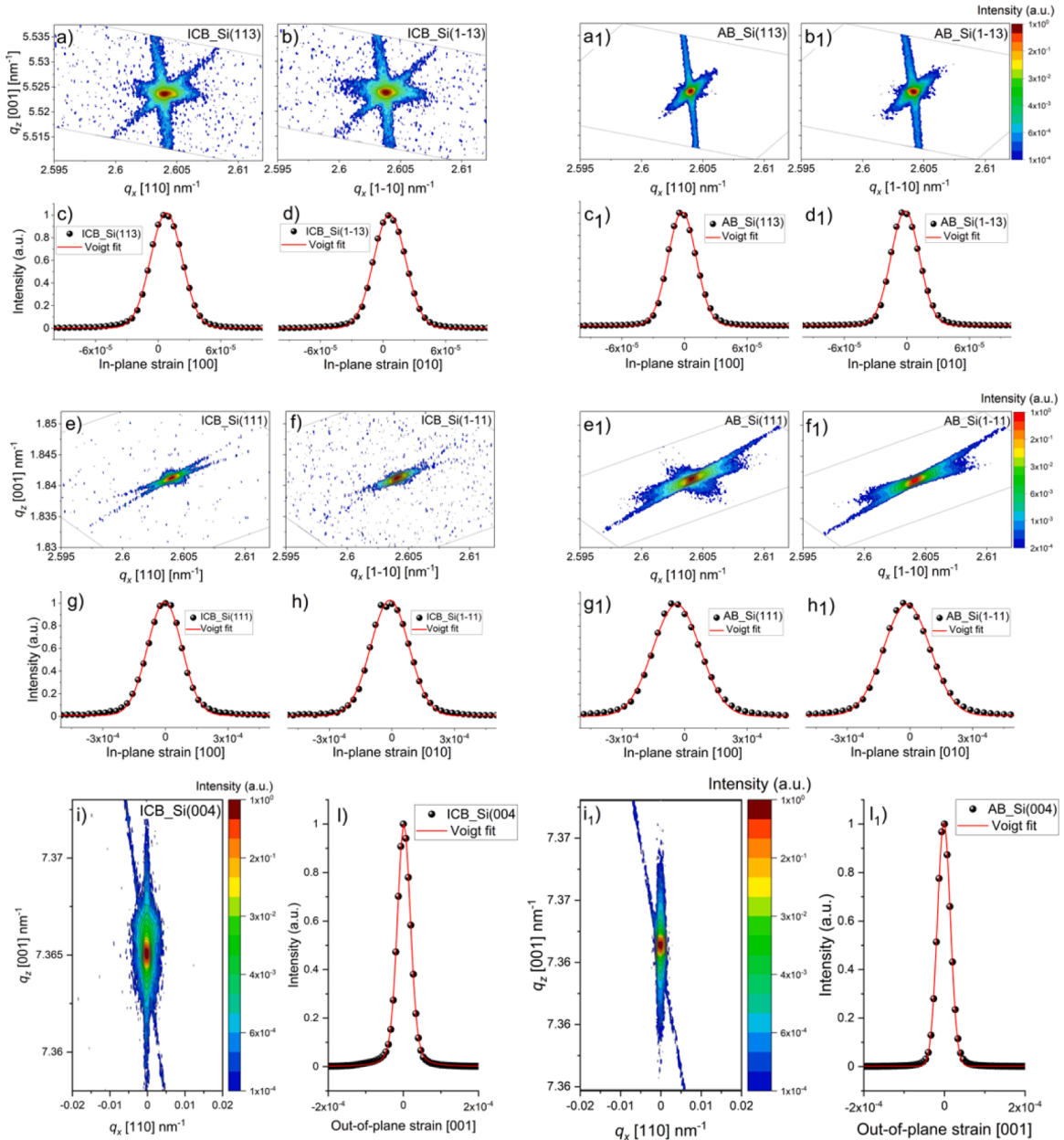


**Fig. 2.** HRXRD analyzes on the ICB and AB assembled samples. From (a) to (l) ICB assembled sample. From (a<sub>1</sub>) to (l<sub>1</sub>) analogous for the AB assembled sample. (a) and (b) Reciprocal Space Maps of the 113 and 1-13 reflections measured in symmetric noncoplanar diffraction geometry; (c) and (d) in-plane components of the lattice strain along with the crystallographic directions [100] and [010] calculated from the lattice strain measured along the [113] and [1-13] crystalline directions. The red line is the Voigt function used to fit the experimental points in black; (e) and (f) Reciprocal Space Maps of the 111 and 1-11 reflections measured in symmetric noncoplanar diffraction geometry. (g) and (h) in-plane components of the lattice strain along the crystallographic directions [100] and [010] calculated from the lattice strain measured along the [111] and [1-11] crystalline directions. The red line is the Voigt function used to fit the experimental points in black; (i) Reciprocal Space Maps of the out-of-plane 004 reflections measured in symmetric coplanar diffraction geometry; (l) out-of-plane component of the lattice strain along the crystallographic direction [004] calculated from the same reflection. From (a<sub>1</sub>) to (l<sub>1</sub>), analogous to the letter with no suffix, related to the AB assembled sample.

the case of our present study, the plane stress is calculated as follows:

$$\sigma_{xy} = \frac{E}{1 - \nu_{xy}} \cdot \varepsilon_x \quad (5)$$

Under the assumption of equibiaxial stress, the in-plane stress can be estimated from the out-of-plane strain. In this case, given the strain along the z-direction ( $\varepsilon_z$ ), the in-plane stress writes

$$\sigma_{xy} = -\frac{E}{2 \cdot \nu_{xy}} \cdot \varepsilon_z \quad (6)$$

### 3. Results and discussion

The perfection of the silicon crystal lattice and the in-plane components of the strain were measured from the inclined reflections, 113 and 1–13, and 111 and 1–11, respectively. Each couple of reflections, 113 and 1–13, for instance, are equivalent in terms of the Bragg's angle and inclination with respect to the sample surface, i.e., the [001] direction, but they are 90° rotated in the azimuthal plane with respect to each other. The strain along a crystalline direction with an inclination angle with respect to the normal direction different from 0° (out-of-plane only) and 90° (in-plane only) has both the in-plane and out-of-plane components. The larger the angle between the normal direction and the measured crystalline direction, the more the in-plane component of the strain becomes predominant over the out-of-plane component. Fig. 2 (a, b) show the RSMs of the 113 and 1–13 reflections, respectively. In Fig. 2(e, f), the 111 and 1–11 reflections are shown, respectively. Fig. 2 (i) shows the RSM of the Si 004 lattice point.

#### 3.1. Anodic bonding

For the sake of clarity, results from samples assembled using the conventional AB technology are discussed first and then compared to the ICB assembled samples.

The broadening of the 113 and 1–13 silicon crystal lattice points in the reciprocal space, in Fig. 2(a<sub>1</sub>, b<sub>1</sub>), are limited in virtue of the high crystalline quality of the silicon single crystal, evidently conserved after the AB process. The broadening extracted from the Voigt fit of the radial scans (coupled 2θ-ω scans) is 0.006° in terms of full-width at the half maximum (FWHM) in both azimuthal directions. The out-of-plane tilt of the atomic planes (ω-RCs) spreads over a range of 0.003° and 0.005° for the 113 and the orthogonal 1–13 reflections, respectively. The Si 111 and its normal reflection in the azimuthal direction, i.e., the Si 1–11, in Fig. 2(e<sub>1</sub>) and 3(f<sub>1</sub>), respectively, show a larger spread of the out-of-plane tilt being both RCs widths equal to 0.011°. The broadening of the 111 lattice point in silicon and other cubic symmetry crystals is often observed and relates to the formation of 60° dislocations in the Si lattice [45].

Fig. 2(c<sub>1</sub>, d<sub>1</sub>, g<sub>1</sub>, h<sub>1</sub>) report 1D profiles of the in-plane component of the lattice strain along with the crystalline directions [100] and [010]. The average in-plane component of the strain was calculated from the lattice strain measured along the [113] and [111] (and azimuthally orthogonal ones) directions, and it is represented by the deviation of the peak center with respect to the zero-strain value. The strain profiles are derived from the radial scans extracted from the RSMs. By a simple conversion based on Bragg's law,

$$\varepsilon_{X-ray, hkl} = \left( \frac{\sin(\theta_{hkl})}{\sin(\theta_{hkl}^0)} \right) - 1$$

the strain along the crystalline direction [hkl] can be calculated from the deviation of the Bragg angle  $\theta_{hkl}$  with respect to its theoretical value  $\theta_{hkl}^0$  (reported in Table 1). The in-plane strain profiles obtained from the 113 and 1–13 reflections are centered at  $-3 \cdot 10^{-6}$  and  $-2 \cdot 10^{-6}$ . Both values are smaller than the incertitude provided by the angular resolution of the 113 reflection in the exploited diffraction geometry, i.e., 0.003°. This translates into a resolution of the in-plane strain component equal to

$\pm 2 \cdot 10^{-5}$ . When the in-plane components of the strain are derived from the 111 and 1–11 reflections, the profiles are centered at  $-3 \cdot 10^{-5}$  and  $-1 \cdot 10^{-5}$  along [100] and [010], respectively. Also, in this case, these values are smaller than the detection limit of the in-plane strain components allowed by the angular resolution on the measurement of the 111 reflection, i.e.,  $\pm 8 \cdot 10^{-5}$ . Under the assumption of plane stress affecting the crystal, the measurable stress has a threshold of  $\pm 4$  MPa when considering the 113 reflection, and  $\pm 14$  MPa if the strain is obtained from the 111 reflection. Accordingly, the residual stress measured at the interface between Si and borosilicate glass bonded by conventional anodic bonding is below 4 MPa.

The measurement of the strain along the [004] out-of-plane direction provides further confirmation of the low stress at the bonding interface. The strain along the [001] should be equal to  $|2 \cdot 10^{-5}|$  when stress with module  $|4 \text{ MPa}|$  is applied along with the X and Y directions. A similar strain would be detectable by the diffraction measurements in a high-resolution setup as the strain-detection limit for the 004 reflections is equal to  $|6 \cdot 10^{-6}|$ . Fig. 2(i<sub>1</sub>) shows the Si 004 lattice point broadening and Fig. 2(l<sub>1</sub>) the corresponding strain profile. The Voigt fit of the measured peak is centered at  $-1 \cdot 10^{-6}$ ; thus, its deviation from the center being smaller than the instrumental strain resolution. Additionally, if an equibiaxial stress assumption is considered, a value of out-of-plane strain equal to the strain resolution arising from the measurement of the 004 reflection, i.e.,  $|6 \cdot 10^{-6}|$ , would relate to in-plane stress equal to  $|1.4 \text{ MPa}|$ . Accordingly, we assume the stress at the bonding interface is below 1 MPa.

#### 3.2. Impulse current bonding (ICB): comparison with the conventional AB technology

Being the Impulse Current Bonding packaging a novel technology, we first focused on the qualification of the bonding through the evaluation of the interface. X-ray micro-CT has been used to obtain images of the two materials bonded at different parts of the sample. Fig. 3(a) shows the sample cross-section where the 600 μm-thick Si wafer has a higher gray value (less absorption), and the part with lower gray value (higher absorption) represents the glass wafer remaining after the etching. It is possible to distinguish between the central part of the sample presenting continuity of the interface and the two outer parts where a lack of bonding is present. The status of the interface in the external part is shown in Fig. 3(a, b). At the edges of the cross-section, the glass appears missing and unbonded to the Si wafer. A black line (air) is clearly visible in Fig. 3(b) by zooming into the sample edge. However, the scanning electron microscopy image in Fig. 3(c) and the optical microscopy image in Fig. 3(d) clarify the reason for the lack of adhesion: the interface has been etched by the hydrofluoric (HF) acid being used for the thinning of the glass wafer. The glass at the edges is clearly corroded, and the color changed, as shown by the optical microscopy image. The HF acid corroded the glass also at the interface with Si compromising the bonding for a length of a few hundred micrometers from the edges, as the SEM micrograph shows. This is the reason for the visible voids from the micro-CT analysis. It does not represent any objecting issue for the bonding technology, which, in turn, confirms its high effectiveness.

For observing the interface status in the center of the sample, a  $5 \times 5 \text{ mm}^2$  ROI has been selected for the local micro-CT analysis, as shown in Fig. 3(e). The 3D-rendering of the local ROI in Fig. 3(f) shows the glass in blue and the silicon in semi-transparent green color and allows to observe the interface in detail, which is indeed devoid of densimetric differences attributable to the presence of cracks or voids. The bonding interface has been evaluated at different points in the local ROI and does not reveal defects as far as allowed by the resolution of the technique; around 1.55 μm for the local CT, as visible in the grey-scale tomographic images in Fig. 3(g). When inspecting the interface at higher

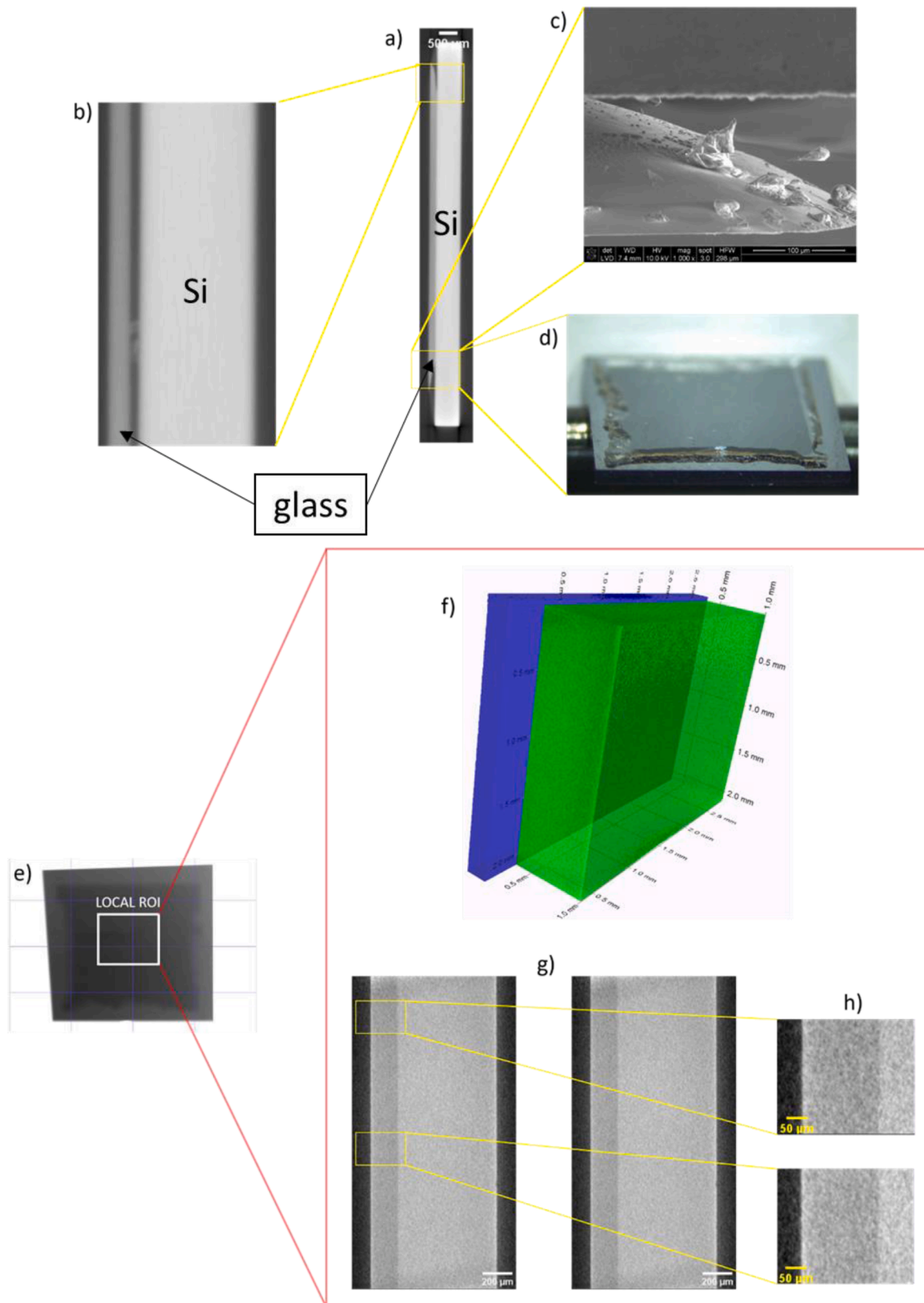


**Fig. 3.** X-ray micro-CT and SEM analyzes on one sample assembled by ICB. (a) radiography of the whole sample cross-section and zoom-in on the area close to the sample edge (representative of both the edges); (b) X-ray micro CT image of the sample edge. (c) SEM micrograph of the sample edge highlighting part of the glass is removed; (d) optical microscopy image of the  $2 \times 2 \text{ cm}^2$  sample. HRXRD were performed at the center of the sample; the length of the illuminated area is 2 cm in the direction orthogonal to the scattering plane and the width is  $600 \mu\text{m}$  in the direction of the scattering plane; (e) full-size X-ray radiography of the sample. The white square points out the sample part where the local CT is performed in an area of  $5 \times 5 \text{ mm}^2$ . (f) 3D-rendering of the bonding interface in the Local CT ROI (semi-transparent green-Si, blue-glass); (g) Local high-resolution X-ray micro CT images of the bonding interface at a different point along the sample cross-section: the resolution is  $1.55 \mu\text{m}$ ; (h) high-magnification local X-ray micro CT image of the bonding interface at different points.

magnification, there are no visible defects affecting the Si/glass bonding interface (Fig. 3(h)). These observations are particularly relevant because the presence of interfacial defects would represent the leading cause of bonding failure and the loss of hermeticity. Furthermore, the bonding interface appears homogeneous in the different points probed, pointing out that the bonding is successful for the entire sample.

From the comparison between Fig. 2(a, b) and ( $a_1$ ,  $b_1$ ), the Si 113 and 1-13 lattice points appear broader for the samples assembled by ICB than for the AB processed. However, the differences in terms of the broadening of the lattice points both in the radial direction (coupled  $2\theta$ - $\omega$  scans) and in the angular direction ( $\omega$ -RCs), are not significant, being smaller than the angular resolution allowed by the technique for the measured reflections, i.e.,  $0.003^\circ$ . The visible broadening of the lattice point in the RSMs involves regions of the reciprocal space where the intensities are already decayed by 3 or 4 orders of magnitude with respect to the Bragg peak maximum intensity. This part of the RSM is clearly not represented in the width of the fitting functions, which relates to the average strain gradient or the spread of the tilt, but involves the diffuse scattering, which relates to the presence of lattice defects. Since the broadening of the lattice point reflects the decrease in the crystal perfection, we quote on a slight reduction of the SCSi lattice perfection in the vicinity of the bonding interface when the ICB technology is performed. This may be due to the accumulation of defects in the near bonding interface region.

The diffuse scattering, i.e., the radiation scattered at angles different from the predicted for the amplitude enhancement due to coherent interference (Bragg angle) and contributing to the peaks tails, is in part generated by the presence of lattice defects. Defects break the coherence of the crystal domains causing the variation of the scattering angle. The integration of the peaks and the weighting of the diffuse scattering with respect to the coherent scattering may provide a quantitative interpretation for the density of crystalline defects present in the crystal. Fig. 4(a, b) show the comparison between the Si 113 rocking curves for the AB and ICB assembled samples, respectively. The total area of the peaks (which includes the coherent and diffuse scattering) and the area related to the coherent scattering alone are reported. In the present approach, we evaluated the area of the peaks coming from the coherent scattering by fitting with a Voigt function (red dotted lines in Fig. 4(a, b)). The total integrated area of each curve has been used as a figure of merit of the total scattered radiation. The weight of the diffuse scattering was evaluated according to the following equation  $A_d = (A_T - A_c) / A_T * 100$ , where  $A_d$  is the percentage of area related to the diffuse scattering,  $A_T$  the total scattering area, and  $A_c$  the peak area fitted by a Voigt function.

The diffuse scattering represents  $1.3 (\pm 0.1) \%$  of the total scattering of the Si 113 of Si bonded by AB. The weight of the diffuse scattering related to the same reflection increases up to  $5.6 (\pm 0.1) \%$  in ICB processed samples. When the Si 1-13 reflection is taken into account, the diffuse scattering weight for the AB and ICB processed samples are  $1.5 (\pm 0.1) \%$  and  $4.7 (\pm 0.1) \%$ , respectively. As for the symmetric Si 004 out-of-plane reflection, the diffuse scattering contributes only  $1.2 (\pm 0.1) \%$  to the total area of the RC peak in AB samples. The weight of the diffuse scattering increases up to  $4.5 (\pm 0.1) \%$  in ICB samples. The diffuse scattering from the Si 111 was not evaluated due to the higher broadness and much lower statistics. These results, resumed in Fig. 4(c), show a clear trend: the ICB processed samples relate to a raised contribution of the incoherent scattering along each crystalline direction in comparison to the analogous AB processed samples. The more significant contribution from the incoherent scattering arises from a higher concentration of lattice defects, most probably at the bonding interface.

The generation of crystalline defects at the bonding interface region alone is not evaluable for the success of the bonding technology. Whatever bonding mechanism relies on the "perturbation" of the crystalline order at the surfaces of the bonded materials. Only by this perturbation, the two separate surfaces become an inseparable interface, composing an interfacial hybrid material by mixing the material of the two surfaces due to diffusion mechanisms, and the bonding process

succeeds. In other words, the presence of a slightly more significant amount of crystal lattice defects at the bonding interface region as it is for ICB technology might also correlate to a thicker hybrid region. This difference is attributed to an increased atomic flow rate at the interface with an impulse current, but no correlation to the effectiveness of the bonding can be concluded yet. Expectation that this difference constituting a positive achievement for ICB with an improved bonding strength could be evaluated in further studies to establish the relationship with the amount of lattice defects quantified in this work.

Independence of the applied technology, lattice defects form and influence the strength of the bonding. Therefore, it is crucial to evaluate the impact of defects on the residual stress at the bonding interface. According to Fig. 2(c, d), the in-plane components of the strain profiles deviate from zero by  $6 \times 10^{-6}$  and  $8 \times 10^{-6}$  for the Si 113 and Si 1-13, respectively. For the AB as well as for the ICB processed samples, these values are smaller than the strain resolution allowed by the angular resolution. Similar results are obtained from the evaluation of the in-plane strain along the [001] and [010] crystal directions obtained from the measurements of the 111 and 1-11 reflections. Here the values of the average in-plane components of the strain are  $-4 \times 10^{-6}$  and  $-1 \times 10^{-5}$ , while the allowed strain resolution is  $8 \times 10^{-5}$ .

Further, the ICB-processed samples were measured for obtaining the strain along with the 004 out-of-plane reflections. Fig. 2(i) shows the Si 004 lattice point broadening. The comparison between Fig. 2(i, i<sub>1</sub>) offers visual confirmation of the larger amount of diffuse scattering affecting the ICB processed silicon diffraction peaks. Also in this case, the broadening does not affect the coherent scattering regions but arising instead from an increased diffuse scattering of the near-Bragg peak.

As above-mentioned, the strain along  $z$  should be equal to  $2 \times 10^{-5}$  when the minimum in-plane stress detectable by our configuration, i.e., 4 MPa, applies. The strain profile is shown in Fig. 2(l) deviates from zero by  $2 \times 10^{-6}$ . Again, this strain value is smaller than the strain resolution allowed by our analytical setup, i.e.,  $|6 \times 10^{-6}|$ . Accordingly, and as well for the AB processed samples, the stress induced by the ICB bonding is below 1 MPa.

These results are highly relevant because they prove that the bonding interface of ICB processed silicon and glass is unaffected by residual stress due to lattice defects, this constituting a remarkably positive characteristic of the novel process in terms of reliability. Table 2 summarizes the features of each measured reflection and offers a direct comparison between the two investigated packaging technologies.

#### 4. Conclusions

We present the first direct evaluation of materials and process-related features for silicon-to-glass bonding obtained by the innovative ICB technology. The influence of the novel design for MEMS assembling on the bonding effectiveness has been evaluated for the presence of interfacial micrometer-sized defects and voids, lattice defects, and defects-induced residual stress at the bonding interface. The methods of choice were HRXRD and X-ray micro-CT allowing the required precision and resolution. Our analytical approach allows the labeling of this new ICB bonding technology with respect to the preservation of the materials system quality being comparable to the well-established AB process.

The residual stress at the bonding interface due to the formation of lattice defects is below 1 MPa. That releases the ICB technology from the general concern related to eventual failure related to the process-induced residual stresses. The presence of lattice defects generated at the bonding interface was also investigated by quantifying the diffuse scattering in the near-Bragg region, which was finally used as a figure of merit of the lattice disorder. The incoherent scattering weight over the total scattering is slightly more in ICB-processed crystals than AB-processed samples. This trend is consistently observed for all measured reflections. Accordingly, the ICB generates a higher density of lattice defects at the interface; however, without a translation into an increase of the residual stress or an interface degradation, which proved



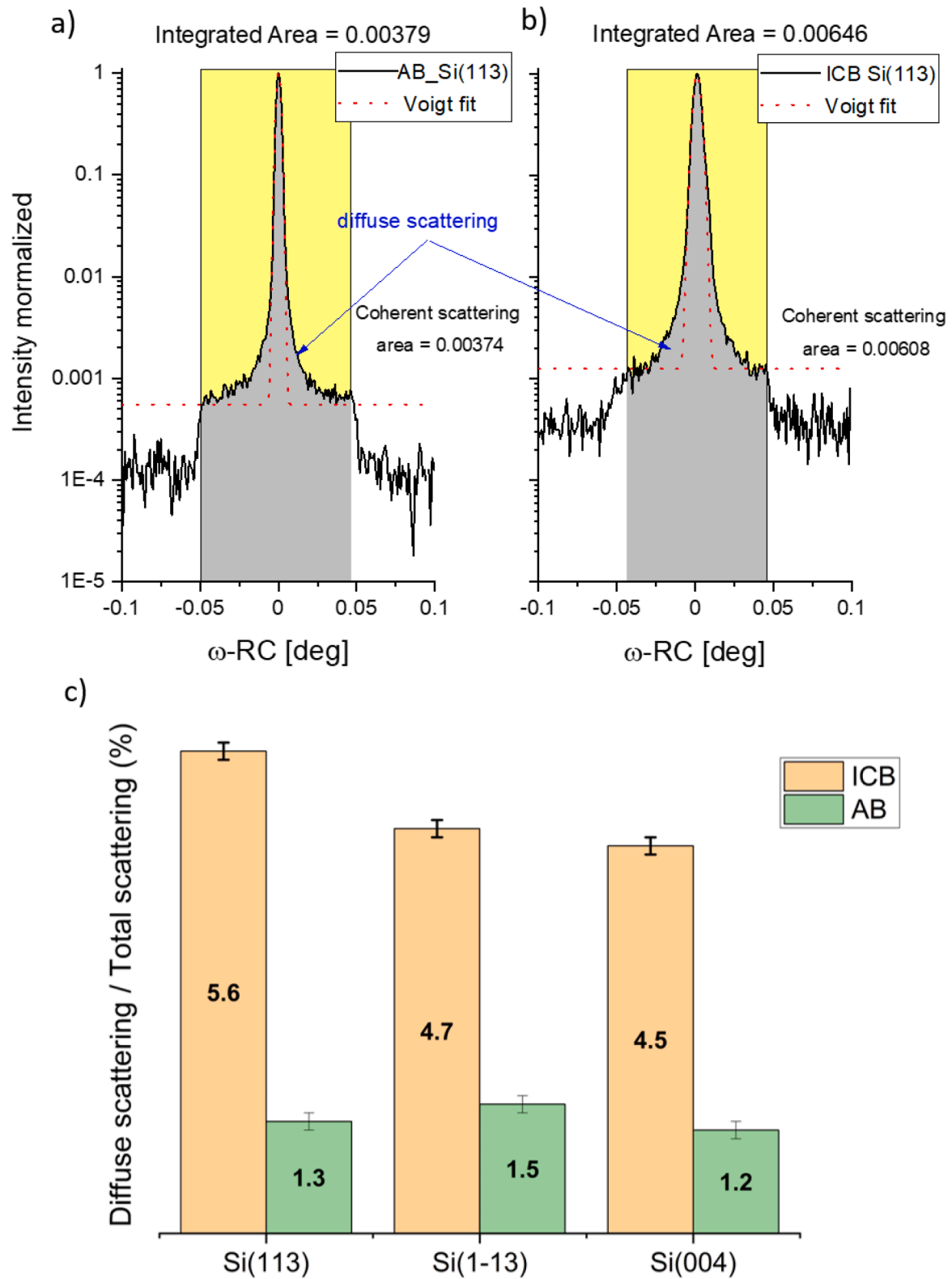


**Fig. 4.** Quantification of the diffuse scattering weight over the total scattering for different measured reflections. (a) RCs of the Si 113 from samples assembled by AB. The total scattering is obtained from the area integrated under the yellow square. The coherent scattering is the area under the Voigt fitting (red dots); (b) RCs of the Si 113 from samples assembled by ICB. The total scattering is obtained from the area integrated under the yellow square. The coherent scattering is the area under the Voigt fitting (red dots); (c) Percentage weight of the diffuse scattering for the three reflection measured by HRXRD, the Si 113, 1-13, and 004. The standard errors were obtained from the fittings over the curve integration and the Voigt fitting, being around  $\pm 0.1\%$ . The orange bars relate to the ICB assembled samples, while the green bars correspond to the AB processed samples.

**Table 2**

Data extracted from the HRXRD analysis on the AB and ICB processed samples. For the reference values, please refer to Table 1. The angular positions are measured on a Si 111 stress-free crystal used as a reference. Accuracies over the widths and positions of the peaks are estimated from the Si 111 stress-free reference crystals (values in Table 1).

Sample	Reflection <i>hkl</i>	Position stress-free Si 111 reference 2 $\theta$ (°)	Position 2 $\theta$ (°)	FWHM 2 $\theta$ (°)	$\omega$ -RC FWHM (°)	Diffuse scattering weight (%) ( $\pm 0.1$ )
AB	113	56.122	56.122	0.007	0.004	1.3
	1-13	56.122	56.122	0.007	0.005	1.5
	111	28.442	28.444	0.008	0.012	
	1-11	28.442	28.443	0.008	0.011	
	004	69.129	69.129	0.008	0.008	1.2
ICB	113	56.122	56.120	0.008	0.006	5.6
	1-13	56.122	56.121	0.008	0.006	4.7
	111	28.442	28.442	0.008	0.004	NA
	1-11	28.442	28.443	0.009	0.010	NA
	004	69.129	69.129	0.007	0.008	4.5

devoid of any imperfection based on the CT analysis. The minor increase of defects in the silicon lattice, is the first measurement of the difference between the two technologies, and is at our opinion related to a specific bonding mechanism for ICB. This analysis however does not provide any information about the lack of reliability of the novel technology, maintaining the general advantage of a low thermal stress induced by the innovative low temperature bonding process.

The ICB technology is up-and-coming due to the advantages it will provide in the microelectronic manufacturing industry with not only the noticeable reduction of both the bonding process temperature and the cycle time but also in its applicability to a wide range of material pairs which will open new fields of applications. In addition, the inherent reduction of the energy consumption in high volume production sectors, especially the MEMS market, could lead to a significant breakthrough in reducing the energy footprint.

In the presented work, we proved for the first time the effectiveness of this novel packaging technology by means of our HRXRD X-ray and micro-CT conjoint approach.

#### CRediT authorship contribution statement

**Aurelio Borzi:** Methodology, Formal analysis, Investigation, Writing – original draft. **Robert Zboray:** Methodology, Formal analysis, Investigation, Writing – original draft. **Simone Dolabella:** Formal analysis, Writing – review & editing. **Sébastien Brun:** Resources, Writing – review & editing. **Florian Telmont:** Resources, Writing – review & editing. **Peter Kupferschmied:** Resources, Writing – review & editing. **Jean-François Le Néal:** Resources, Writing – review & editing. **Pedrag Drljaca:** Resources, Writing – review & editing. **Gianni Fiorucci:** Writing – review & editing, Project administration, Funding acquisition. **Alex Dommann:** Writing – review & editing, Supervision. **Antonia Neels:** Conceptualization, Supervision, Resources, Project administration, Funding acquisition, Writing – review & editing.

#### Declaration of Competing Interest

The authors declare to have no conflicts of interest. The authors declare that they have no known competing financial interests or personal relationships that could have appeared to influence the work reported in this paper.

#### Acknowledgments

Financial support has been provided by the Swiss Innosuisse project ATOM "Assembly TechnOlogy for MEMS" (No. 37572.1 IP-ENG). We are grateful for the financial support provided by the Swiss National Science Foundation for the project Nano-QX "Novel monolithic Si NEMS: Study and correlation of structural and physical behavior" (No. 169257). Authors are grateful to Federica Orellana for the graphical description of

the X-ray micro-CT experimental setup.

#### References

- [1] Global Smart Sensors Market | 2021 - 26 | Industry share, size, growth - mordor intelligence, (n.d.). <https://www.mordorintelligence.com/industry-reports/global-smart-sensors-market-industry> (accessed September 20, 2021).
- [2] S.-H. Choa, Reliability of MEMS packaging: vacuum maintenance and packaging induced stress, *Microsyst. Technol.* 11 (2005) 1187–1196, <https://doi.org/10.1007/s00542-005-0603-8>.
- [3] O. Brand, H. Baltes, Microsensor packaging, *Microsyst. Technol.* 7 (2002) 205–208, <https://doi.org/10.1007/s005420100110>.
- [4] G. Kelly, J. Alderman, C. Lyden, J. Barrett, Microsystem packaging: lessons from conventional low cost IC packaging, *J. Micromech. Microeng.* 7 (1997) 99–103, <https://doi.org/10.1088/0960-1317/7/3/004>.
- [5] R. Gooch, T. Schimert, Low-cost wafer-level vacuum packaging for MEMS, *MRS Bull.* 28 (2003) 55–59, <https://doi.org/10.1557/mrs2003.18>.
- [6] A.V. Chavan, K.D. Wise, Batch-processed vacuum-sealed capacitive pressure sensors, *J. Microelectromech. Syst.* 10 (2001) 580–588, <https://doi.org/10.1109/84.967381>.
- [7] T. Corman, P. Enoksson, G. Stemme, Gas damping of electrostatically excited resonators, *Sens. Actuators A* 61 (1997) 249–255, [https://doi.org/10.1016/S0924-4247\(97\)80270-1](https://doi.org/10.1016/S0924-4247(97)80270-1).
- [8] D. Liu, D. Luo, A.N. Iqbal, K.W.P. Orr, T.A.S. Doherty, Z.H. Lu, S.D. Stranks, W. Zhang, Strain analysis and engineering in halide perovskite photovoltaics, *Nat. Mater.* (2021), <https://doi.org/10.1038/s41563-021-01097-x>.
- [9] S. Kobayashi, K. Ohwada, T. Hara, T. Oguchi, Y. Asaji, K. Yaji, Double-frame silicon gyroscope packaged under low pressure by wafer bonding, *IEEE Trans. Sens. Micromach.* 120 (2000) 111–115, <https://doi.org/10.1541/ieejsmas.120.111>.
- [10] M. Esashi, N. Ura, Y. Matsumoto, Anodic bonding for integrated capacitive sensors, in: *Proceedings of the IEEE Micro Electro Mechanical Systems, IEEE, Travemunde, Germany, 1992*, pp. 43–48, <https://doi.org/10.1109/MEMSYS.1992.187688>.
- [11] G. Wallis, D.I. Pomerantz, Field assisted glass-metal sealing, *J. Appl. Phys.* 40 (1969) 3946–3949, <https://doi.org/10.1063/1.1657121>.
- [12] M.M. Visser, J.A. Plaza, D.T. Wang, A.B. Hanneborg, Chemical analysis of bonded and debonded silicon-glass interfaces, *J. Micromech. Microeng.* 11 (2001) N1–N6, <https://doi.org/10.1088/0960-1317/11/5/401>.
- [13] Jeung Sang Go, Young-Ho Cho, Experimental evaluation of anodic bonding process using Taguchi method for maximum interfacial fracture toughness, in: *Proceedings of the MEMS 98. IEEE. Eleventh Annual International Workshop on Micro Electro Mechanical Systems. An Investigation of Micro Structures, Sensors, Actuators, Machines and Systems (Cat. No.98CH36176)*, IEEE, Heidelberg, Germany, 1998, pp. 318–321, <https://doi.org/10.1109/MEMSYS.1998.659775>.
- [14] T. Rogers, Considerations of anodic bonding for capacitive type silicon/glass sensor fabrication, *J. Micromech. Microeng.* 2 (1992) 164–166, <https://doi.org/10.1088/0960-1317/2/3/008>.
- [15] Lithography and Bonding equipment for More than Moore 2021, I-Micronews, 2021 n.d. <https://www.i-micronews.com/products/lithography-and-bonding-equipment-for-more-than-moore-2021/> (accessed September 20).
- [16] S.K. Estreicher, D.J. Backlund, C. Carbogno, M. Scheffler, Activation energies for diffusion of defects in silicon: the role of the exchange-correlation functional, *Angew. Chem. Int. Ed.* 50 (2011) 10221–10225, <https://doi.org/10.1002/anie.201100733>.
- [17] I.E. Collings, M. Bykov, E. Bykova, M. Hanfland, S. van-Smaalen, L. Dubrovinsky, N. Dubrovinskaia, Disorder–order transitions in the perovskite metal–organic frameworks [(CH<sub>3</sub>)<sub>2</sub>NH<sub>2</sub>][M(HCOO)<sub>3</sub>] at high pressure, *CrystEngComm* 20 (2018) 3512–3521, <https://doi.org/10.1039/C8CE00617B>.
- [18] M. Birkholz, *Thin Film Analysis by X-Ray Scattering*, 1st ed., Wiley, 2005 <https://doi.org/10.1002/3527607595>.
- [19] J.I. Langford, A.J.C. Wilson, Scherrer after sixty years: a survey and some new results in the determination of crystallite size, *J. Appl. Crystallogr.* 11 (1978) 102–113, <https://doi.org/10.1107/S0021889878012844>.

- [20] A. Monshi, M.R. Foroughi, M.R. Monshi, Modified scherrer equation to estimate more accurately nano-crystallite size using XRD, *WJNSE* 02 (2012) 154–160, <https://doi.org/10.4236/wjnse.2012.23020>.
- [21] A. Borzi, S. Dolabella, W. Szmyt, J. Geler-Kremer, S. Abel, J. Fompeyrine, P. Hoffmann, A. Neels, Microstructure analysis of epitaxial BaTiO<sub>3</sub> thin films on SrTiO<sub>3</sub>-buffered Si: strain and dislocation density quantification using HRXRD methods, *Materialia* 14 (2020), 100953, <https://doi.org/10.1016/j.mtla.2020.100953>.
- [22] H.-M. Wang, J.-P. Zhang, C.-Q. Chen, Q. Fareed, J.-W. Yang, M.A. Khan, AlN/AlGaIn superlattices as dislocation filter for low-threading-dislocation thick AlGaIn layers on sapphire, *Appl. Phys. Lett.* 81 (2002) 604–606, <https://doi.org/10.1063/1.1494858>.
- [23] T. Metzger, R. Höppler, E. Born, O. Ambacher, M. Stutzmann, R. Stömmers, M. Schuster, H. Göbel, S. Christiansen, M. Albrecht, H.P. Strunk, Defect structure of epitaxial GaN films determined by transmission electron microscopy and triple-axis X-ray diffractometry, *Philos. Mag. A* 77 (1998) 1013–1025, <https://doi.org/10.1080/01418619808221225>.
- [24] S. Dolabella, A. Borzi, A. Dommann, A. Neels, Lattice strain and defects analysis in nanostructured semiconductor materials and devices by high-resolution X-ray diffraction: theoretical and practical aspects, *Small Methods* (2021), 2100932, <https://doi.org/10.1002/smt.202100932>.
- [25] V.S. Kopp, V.M. Kaganer, B. Jenichen, O. Brandt, Analysis of reciprocal space maps of GaN(0001) films grown by molecular beam epitaxy, *J. Appl. Crystallogr.* 47 (2014) 256–263, <https://doi.org/10.1107/S1600576713032639>.
- [26] A. Benediktovich, A. Zhylik, T. Ulyanenkova, M. Myronov, A. Ulyanenkova, Characterization of dislocations in germanium layers grown on (011)- and (111)-oriented silicon by coplanar and noncoplanar X-ray diffraction, *J. Appl. Crystallogr.* 48 (2015) 655–665, <https://doi.org/10.1107/S1600576715005397>.
- [27] V. Lashkaryov, Institute of semiconductor physics, NAS of Ukraine, 41, prospect Nauky, 03028 Kyiv, Ukraine, N.V. Safriuk, X-ray diffraction investigation of GaN layers on Si(111) and Al<sub>2</sub>O<sub>3</sub> (0001) substrates, *Semicond. Phys. Quantum Electron. Optoelectron.* 16 (2013) 265–272, <https://doi.org/10.15407/spqeo16.03.265>.
- [28] P.F. Fewster, Multicrystal X-ray diffraction of heteroepitaxial structures, *Appl. Surf. Sci.* 50 (1991) 9–18, [https://doi.org/10.1016/0169-4332\(91\)90133-5](https://doi.org/10.1016/0169-4332(91)90133-5).
- [29] P.F. Fewster, Advances in the structural characterisation of semiconductor crystals by X-ray scattering methods, *Prog. Cryst. Growth Charact. Mater.* 48–49 (2004) 245–273, <https://doi.org/10.1016/j.pcrysgrow.2005.03.001>.
- [30] S. Dolabella, R. Frison, G.A. Chahine, C. Richter, T.U. Schullij, Z. Tasdemir, B. E. Alaca, Y. Leblebici, A. Dommann, A. Neels, Real- and Q-space travelling: multi-dimensional distribution maps of crystal-lattice strain ( $\epsilon_{044}$ ) and tilt of suspended monolithic silicon nanowire structures, *J. Appl. Crystallogr.* 53 (2020) 58–68, <https://doi.org/10.1107/S1600576719015504>.
- [31] O. Yildirim, A. Borzi, C.V. Falub, H. Rohrmann, D. Jaeger, M. Rechsteiner, D. Schneider, A. Neels, H.J. Hug, M.A. Marioni, Tuning the microstructure of the Pt layers grown on Al<sub>2</sub>O<sub>3</sub> (0001) by different sputtering methods, *Scr. Mater.* 194 (2021), 113689, <https://doi.org/10.1016/j.scriptamat.2020.113689>.
- [32] A. Schifferle, A. Dommann, A. Neels, *In situ* MEMS testing: correlation of high-resolution X-ray diffraction with mechanical experiments and finite element analysis, *Sci. Technol. Adv. Mater.* 18 (2017) 219–230, <https://doi.org/10.1080/14686996.2017.1282800>.
- [33] A. Neels, A. Dommann, P. Niedermann, C. Farub, H. von-Känel, E. Zschech, S. Ogawa, P.S. Ho, Advanced Stress, Strain And Geometrical Analysis In Semiconductor Devices, Bad Schandau, Germany), 2010, pp. 114–119, <https://doi.org/10.1063/1.3527115>.
- [34] E. Burden, Y. Oh, B. Mummareddy, D. Negro, P. Cortes, A. Du-Plessis, E. MacDonald, J. Adams, F. Li, R. Rojas, Unit cell estimation of volumetrically-varying permittivity in additively-manufactured ceramic lattices with X-ray computed tomography, *Mater. Des.* (2021), 110032, <https://doi.org/10.1016/j.matdes.2021.110032>.
- [35] S. Van-Offenwert, V. Cnudde, M. Boone, T. Bultreys, Fast micro-computed tomography data of solute transport in porous media with different heterogeneity levels, *Sci Data* 8 (2021) 18, <https://doi.org/10.1038/s41597-021-00803-3>.
- [36] L. Hong, P. Zhang, D. Liu, P. Gao, B. Zhan, Q. Yu, L. Sun, Effective segmentation of short fibers in glass fiber reinforced concrete's X-ray images using deep learning technology, *Mater. Des.* 210 (2021), 110024, <https://doi.org/10.1016/j.matdes.2021.110024>.
- [37] A.Q.R. Baron, S.L. Ruby, Time resolved detection of X-rays using large area avalanche photodiodes, *Nucl. Instrum. Methods Phys. Res. Sect. A Accel. Spectrom. Detect. Assoc. Equip.* 343 (1994) 517–526, [https://doi.org/10.1016/0168-9002\(94\)90232-1](https://doi.org/10.1016/0168-9002(94)90232-1).
- [38] R. Farrell, K. Vanderpuye, G. Entine, M.R. Squillante, High resolution, low energy avalanche photodiode X-ray detectors, *IEEE Trans. Nucl. Sci.* 38 (1991) 144–147, <https://doi.org/10.1109/23.289288>.
- [39] A. du-Plessis, I. Yadroitsava, I. Yadroitsev, Effects of defects on mechanical properties in metal additive manufacturing: a review focusing on X-ray tomography insights, *Mater. Des.* 187 (2020), 108385, <https://doi.org/10.1016/j.matdes.2019.108385>.
- [40] A. Borzi, R. Zboray, S. Dolabella, J.F. Le-Neal, P. Drljaca, G. Fiorucci, A. Dommann, A. Neels, A holistic X-ray analytical approach to support sensor design and fabrication: strain and cracking analysis in wafer bonding process, *Mater. Des.* (2021), 110052, <https://doi.org/10.1016/j.matdes.2021.110052>.
- [41] NIST X-ray form factor, attenuation, and scattering tables main page, (n.d.). <https://physics.nist.gov/PhysRefData/FFast/html/form.html> accessed March 23, 2021.
- [42] Stress, Strain, and Structural Dynamics, Elsevier, 2005, <https://doi.org/10.1016/B978-0-12-787767-9.X5000-4>.
- [43] J. Kim, D. Cho, R.S. Muller, E. Obermeier, Why is (111) silicon a better mechanical material for MEMS?, *Transducers '01 Eurosensors XV* Springer, Berlin Heidelberg, 2001, pp. 662–665, [https://doi.org/10.1007/978-3-642-59497-7\\_157](https://doi.org/10.1007/978-3-642-59497-7_157).
- [44] L. Zhang, R. Barrett, P. Cloetens, C. Detlefs, M. Sanchez-del-Rio, Anisotropic elasticity of silicon and its application to the modelling of X-ray optics, *J. Synchrotron Radiat.* 21 (2014) 507–517, <https://doi.org/10.1107/S1600577514004962>.
- [45] J.P. Hirth, A brief history of dislocation theory, *MTA* 16 (1985) 2085–2090, <https://doi.org/10.1007/BF02670413>.